Yulia Grebenyuk, Michael E. Dreyer

Wicking of liquid nitrogen into superheated porous structures

Journal Article	as:	peer-reviewed accepted version (Postprint)
DOI of this document*(secondary publication):		https://doi.org/10.26092/elib/2468
Publication date of this document:		19/09/2023

* for better findability or for reliable citation

Recommended Citation (primary publication/Version of Record) incl. DOI:

Yulia Grebenyuk, Michael E. Dreyer,
Wicking of liquid nitrogen into superheated porous structures,
Cryogenics, Volume 78, 2016, Pages 27-39, ISSN 0011-2275,
https://doi.org/10.1016/j.cryogenics.2016.05.008

Wicking of liquid nitrogen into superheated porous structures

Yulia Grebenyuk *, Michael E. Dreyer

Center of Applied Space Technology and Microgravity (ZARM), University of Bremen, Am Fallturm, 28359 Bremen, Germany

ARTICLE INFO

Article history:
Received 14 January 2016
Received in revised form 6 May 2016
Accepted 9 May 2016
Available online 26 May 2016

Keywords:
Wicking
Cryogenic liquids
Imbibition
Porous structures
Capillary pressure

ABSTRACT

Evaporation in porous elements of liquid–vapor separation devices can affect the vapor-free cryogenic propellant delivery to spacecraft engines. On that account, the capillary transport of a cryogenic liquid subjected to evaporation needs to be understood and assessed. We investigate wicking of liquid nitrogen at saturation temperature into superheated porous media. A novel test facility was built to perform wicking experiments in a one-species system under non-isothermal conditions. A setup configuration enabled to define the sample superheat by its initial position in a stratified nitrogen vapor environment inside the cryostat. Simultaneous sample weight and temperature measurements indicated the wicking front velocity. The mass of the imbibed liquid nitrogen was determined varying the sample superheat, geometry and porous structure. To the author's extent of knowledge, these are the first wicking experiments performed with cryogenic fluids subjected to evaporation using the weight–time measurement technique. A one-dimensional macroscopic model describes the process theoretically. Results revealed that the liquid loss due to evaporation at high sample superheats leads to only a slight imbibition rate decrease. However, the imbibition rate can be greatly affected by the vapor flow created due to evaporation that counteracts the wicking front propagation.

1. Introduction

Cryogenic fluids are widely used in the spaceflight community for high performance propulsion systems. Liquid oxygen and hydrogen are the most common cryogenic propellants. Vapor-free propellant delivery to the engines is of importance for all space mission stages. In the absence of gravity, however, liquid–gas separation becomes challenging. For that reason propellant management devices (PMD) can be implemented inside propellant tanks. Capillary pressure driven flow is an effective solution for the vapor-free liquid transport. Based on this principle, PMDs with porous screen elements [1–3] were designed. A screen PMD, or a screen channel liquid acquisition device (LAD), includes several porous elements that get saturated with a liquid and ensure the liquid transport through them due to the capillary pressure. Vapor ingestion is blocked unless the screen bubble point pressure is not exceeded. An influence of the screen parameters on the LAD performance was investigated in [4–6]. Furthermore, venting might be necessary during ballistic flight phases which could lead to liquid expulsion via the gas ports of upper stage propellant tanks. A gas phase port separator was designed to prevent this undesired effect [7]. The device includes double porous screen elements which shall avoid the expulsion of liquid propellant during venting. A double porous screen element concept and a theoretical model are given in [8].

Evaporation in porous elements can diminish the performance of liquid–vapor separation devices or even lead to their operation failure. Some studies were performed to investigate this effect for storable liquids [9,10]. Cryogenic liquids are characterized by low surface tension values and low normal boiling point temperature. For that reason wicking of cryogenic liquids subjected to evaporation requires a thorough investigation and analysis.

Few studies have been done to understand the behavior of cryogenic fluids in porous structures. Zhang et al. [11] demonstrated wicking of liquid nitrogen with a sintered, multi-layer, porous lamination of metal wire in an open cryogenic chamber. Local temperatures of porous and non-porous samples identical in geometry and material were measured by sensors allocated along the sample length. The saturation of the porous sample with liquid nitrogen changed its temperature response to external heating at the sample top. That indicated the liquid presence in the porous structure. Choi et al. [12] studied the flow phenomena of liquid nitrogen subjected to evaporation in glass wool porous media. Experiments were performed to obtain temperature and pressure distributions in the specimens and, thus, to evaluate the tendency of propagation of the liquid-saturated region in porous media. Some numerical simulations were conducted and compared to experimental results. Vanderlaan and Van Sciver [13,14] investigated different

* Corresponding author.
E-mail addresses: yulia.grebenyuk@zarm.uni-bremen.de (Y. Grebenyuk), michael.dreyer@zarm.uni-bremen.de (M.E. Dreyer).

http://dx.doi.org/10.1016/j.cryogenics.2016.05.008

Nomenclature

Latin letters

A	cross section area of a sample (m^2)
K	permeability (m^2)
L	length (m)
P	weight (N)
R	pore radius (m)
T	temperature (K)
b	parameter of Eq. (13) ($s\ m^{-2}$)
c	parameter of Eq. (13) (m^{-1})
c_P	specific heat capacity at constant pressure ($J\ kg^{-1}\ K^{-1}$)
c_V	specific heat capacity at constant volume ($J\ kg^{-1}\ K^{-1}$)
d	diameter (m)
g	gravity constant ($m\ s^{-2}$)
h	height (m)
j	mass flux ($kg\ s^{-1}\ m^{-2}$)
m	mass (kg)
n_1	parameter of Eq. (13) (–)
n_2	parameter of Eq. (13) (m^{-1})
t	time (s)
u	interstitial velocity ($m\ s^{-1}$)
w	width (m)

Greek letters

ϵ	parameter of Eq. (13) (–)
λ	thermal conductivity ($W\ m^{-1}\ K^{-1}$)
μ	dynamic viscosity (Pa s)
ϕ	porosity (–)
ρ	density ($kg\ m^{-3}$)
σ	surface tension ($N\ m^{-1}$)
θ	static contact angle (°)
Δh	latent heat of evaporation ($J\ kg^{-1}$)

Subscripts

0	initial at a sample bottom
1	first
2	second
L	liquid
SL	sample top
S	solid
V	vapor
eq	equilibrium
ev	evaporation
s	static

flow regimes of superfluid helium through a random pack of uniform size polyethylene spheres. Pressure and temperature drops across a porous medium were measured and computed for different heat inputs. Similar heat transfer studies have been conducted by Allain et al. [15]. A series of experiments with liquid hydrogen, oxygen and nitrogen was performed by Hartwig et al. [16–18] to determine the bubble point pressure of metallic screen meshes. The authors investigated the impact of a screen mesh type, liquid temperature and pressure, and type of pressurization gas.

Nevertheless, to the author's extent of knowledge no experiments have been performed and no theoretical models proposed for a cryogenic liquid subjected to evaporation to assess a key wicking parameter, the imbibition rate. This parameter can be characterized by measuring the mass increase of the porous structure during the imbibition. In case of homogeneous porous media, the imbibition rate can also be characterized via the height increase of the liquid column contained in the porous structure.

In the present work, we investigate wicking of liquid nitrogen at saturation temperature into vertically oriented superheated homogeneous porous media. A novel test facility was built to perform wicking experiments in a one-species system under pre-defined non-isothermal conditions. The mass of the imbibed liquid nitrogen was determined varying the sample superheat, geometry and porous structure. To the author's extent of knowledge these are the first wicking experiments performed with cryogenic fluids using the weight–time measurement technique. A one-dimensional macroscopic wicking model is proposed to evaluate the impact of the porous sample superheat, geometrical and structural characteristics. Furthermore, simultaneous weight and sample temperature measurements indicate the wicking front velocity during the imbibition.

2. Wicking model

Recently, several microscopic models were proposed to characterize a phase change at the liquid–vapor interface in porous media. They imply a pore-scale analysis of the evaporating liquid meniscus using the volume of fluid method [19,20] or the lattice Boltzmann method [21]. Both methods, however, anticipate high computational power costs that currently disable their experimental validation. Aiming to reduce computational power required for simulations, pore network models [22] and their combinations with microscopic models [23] were developed. Nonetheless, only a qualitative validation of some of the proposed models was performed in visualization experiments. Meanwhile, macroscopic or continuum wicking models proved to be a simple and reliable tool for the capillary transport prediction in homogeneous porous media under isothermal conditions. They require minimum computational power and are applicable to perform predictions for lab-scale samples and industrial porous elements. These models are based on averaging of porous media via the introduction of macroscopic parameters: porosity, characteristic pore size and permeability. We propose a macroscopic model for non-isothermal wicking that accounts for evaporation occurring at the wicking front due to the heat transfer between superheated porous media and cryogenic liquid at saturation temperature.

We use the analogy of the flow through porous media to the flow through a bundle of capillary tubes. Such an analogy is inherent to the bundle of capillary tubes macroscopic models. Thus, the momentum balance for isothermal wicking reads as the interaction of the capillary pressure, inertia, viscous forces and hydrostatic pressure (e.g. in [24,25])

$$\frac{2\sigma\cos\theta}{R_s} = \rho_L \frac{d(h\dot{h})}{dt} + \frac{\phi\mu\dot{h}h}{K} + \rho_L g h. \tag{1}$$

Here, the viscous term is given by Darcy's law for porous media. For purely viscous flow Eq. (1) transforms into the Lucas–Washburn equation [26,27]. A good overview of the capillary rise stages in a tube and dominant forces at the stages is given by Stange et al. [28]. Fries and Dreyer [29] predicted the transition time for each stage. As shown in these papers, the purely inertial stage is relevant for early times. In case of small capillaries, for later times the inertia effect vanishes. Therefore, for the capillary transport in porous media many authors neglect inertia and focus on the viscous and gravitational stages. The viscous-gravitational capillary rise in

porous media under isothermal conditions was investigated in [26,30,31].

We study the non-isothermal imbibition of a cryogenic liquid at saturation temperature into a porous sample. The dry solid structure of the vertically oriented sample is superheated with regard to the liquid temperature. The superheat is in accordance with a linear temperature gradient along the sample length. Thus, the local temperature of the dry solid structure T_S is defined by the temperature gradient $\Delta T_S/L$ and the initial temperature at the sample bottom T_0 as

$$T_S = T_0 + \frac{\Delta T_S}{L} h. \tag{2}$$

Due to the heat transfer between superheated porous structure and cryogenic liquid, a certain amount of liquid evaporates at the wicking front. We assume that the vapor created due to evaporation escapes through the lateral sides of the porous sample and, therefore, has no influence on the wicking process. Hence, the momentum balance for the capillary rise of a liquid evaporating in porous media states

$$\frac{2\sigma\cos\theta}{R_s} = \frac{\phi\mu_L}{K} h u_L + \rho_L g h, \tag{3}$$

where u_L is the interstitial velocity of the liquid. Evaporation changes the relationship between u_L and the imbibition rate $\dot{h}$ that were equal to each other in the isothermal case in Eq. (1). A mass balance gives this relationship for the case with evaporation at the wicking front as follows

$$\rho_L\left(u_L - \frac{\mathrm{d}h}{\mathrm{d}t}\right) = \rho_V\left(u_V - \frac{\mathrm{d}h}{\mathrm{d}t}\right) = j_{ev}, \tag{4}$$

where j_{ev} is the evaporative mass flux. From Eq. (4) the interstitial velocity of liquid is given as

$$u_L = \dot{h} + \frac{j_{ev}}{\rho_L}. \tag{5}$$

In [32,33] the similar approach is described for the capillary rise in a tube.

To evaluate the evaporative mass flux, we suppose that the heat needed to cool down the superheated solid structure is taken from the latent heat of evaporation. Thus, the heat needed to cool an infinitely slim layer dh of the solid structure from its local temperature T_S at the wicking front to the saturation temperature of liquid T_L is

$$\frac{\mathrm{d}q}{\mathrm{d}t} = \rho_S c_S (T_S - T_L)(1-\phi) A \frac{\mathrm{d}h}{\mathrm{d}t}, \tag{6}$$

and the latent heat of evaporated liquid is

$$\frac{\mathrm{d}q}{\mathrm{d}t} = \Delta h_v \phi A j_{ev}. \tag{7}$$

Table 1
List of the parameters of Eq. (13).

Parameter	Equation	Physical meaning
ϵ	$\frac{1-\phi}{\phi}$	–
b	$\frac{\phi R_s}{K}\frac{\mu_L}{2\sigma\cos\theta}$	$\frac{\text{viscous forces}}{\text{capillary pressure}}$
c	$R_s\frac{\rho_L g}{2\sigma\cos\theta}$	$\frac{\text{gravity}}{\text{capillary pressure}}$
n_1	$\frac{\rho_S}{\rho_L}\frac{c_S(T_0-T_L)}{\Delta h_v}$	$\frac{\text{sensible heat}}{\text{latent heat of evaporation}}$
n_2	$\frac{\rho_S}{\rho_L}\frac{c_S}{\Delta h_v}\frac{\Delta T_S}{L}$	temperature gradient impact

Rearranging Eqs. (6) and (7), one obtains the evaporative mass flux as follows

$$j_{ev} = \frac{\rho_S c_S (T_S - T_L)(1-\phi)}{\phi \Delta h_v}\frac{\mathrm{d}h}{\mathrm{d}t}. \tag{8}$$

Assuming the heat conduction in the dry solid structure being much slower than the wicking process, we substitute its initial temperature distribution given in Eq. (2) to Eq. (8) that yields

$$j_{ev} = \frac{1-\phi}{\phi}\left(\frac{\rho_S c_S (T_0 - T_L)}{\Delta h_v} + \frac{\rho_S c_S}{\Delta h_v}\frac{\Delta T_S}{L} h\right)\frac{\mathrm{d}h}{\mathrm{d}t}. \tag{9}$$

In order to simplify the equations, we introduce the parameters summarized in Table 1. Using these parameters and substituting Eq. 9 to Eq. 5, one obtains the interstitial velocity of liquid as

$$u_L = \dot{h} + \epsilon n_1 \dot{h} + \epsilon n_2 h \dot{h}. \tag{10}$$

The momentum balance Eq. (3) with the parameters introduced in Table 1 transforms into

$$1 = ch + bhu_L. \tag{11}$$

Substituting Eq. (10) to Eq. (11), one obtains a final equation for the capillary rise of a cryogenic liquid in superheated porous media with evaporation at the wicking front as

$$1 = ch + bh\dot{h}(1 + \epsilon(n_1 + n_2 h)). \tag{12}$$

Integrating Eq. (12) yields the analytic solution in implicit form as follows

$$t(h) = -\frac{b\epsilon n_2}{2c}h^2 - \frac{b}{c}\left(1 + \epsilon\left(n_1 + \frac{n_2}{c}\right)\right)\left(h + \frac{1}{c}\ln(1-ch)\right). \tag{13}$$

More details on the derivation of Eq. (13) are provided in the Appendix.

Eq. (13) with $n_1 = n_2 = 0$ represents a solution for the viscous-gravitational capillary rise in porous media under isothermal conditions given in [26,34]

$$t(h) = -\frac{b}{c}\left(h + \frac{1}{c}\ln(1-ch)\right). \tag{14}$$

3. Material

3.1. Porous media

Experiments were performed with sintered glassfilter elements of porous structures (ROBU Glasfilter-Geraete, Germany). The solid material of the structures was specified as borosilicate glass 3.3. Some thermophysical properties of borosilicate glass are summarized in Table 2.

Samples of two geometries were chosen: cylindrical samples of a larger cross-section area and rectangular samples of a smaller cross-section area. That was done in order to investigate a possible impact of the vapor flow created above the wicking front. Geometrical characteristics of the samples are summarized in Table 3.

The porous structures were of two different characteristic pore sizes. In further experiments the static pore radius was determined. Samples with the static pore radius of 19.7 μm are referred to as R19 or C19, where R stands for rectangular and C for cylindrical samples. Correspondingly, samples with the static pore radius

Table 2
Thermophysical properties of borosilicate glass at room temperature and saturation temperature of nitrogen at 101,325 Pa [41].

T (K)	ρ_S (kg m^{-3}) 10^3	c_S (J kg^{-1} K^{-1}) 10^3	λ_S (W m^{-1} K^{-1})
300	2.23	0.8	1.13
77.355	2.23	0.25	0.5

Table 3
Geometrical characteristics and macroscopic parameters of the porous samples.

Sample	w_1 (m) 10^{-3}	w_2 (m) 10^{-3}	d (m) 10^{-3}	A (m^2) 10^{-6}	L (m) 10^{-3}	ϕ (–)	R_s (m) 10^{-6}	K (m^2) 10^{-12}
R19	15	8	–	120	80	0.40 ± 0.02	19.7 ± 0.4	1.52 ± 0.06
R12	15	10	–	150	80	0.44 ± 0.02	12.3 ± 0.3	0.91 ± 0.04
R12T	15	10	–	150	80	0.44 ± 0.02	12.3 ± 0.3	0.91 ± 0.04
C19	–	–	30	706.5	50	0.35 ± 0.02	19.7 ± 0.4	1.27 ± 0.12
C12	–	–	30	706.5	50	0.31 ± 0.02	12.3 ± 0.3	0.34 ± 0.06

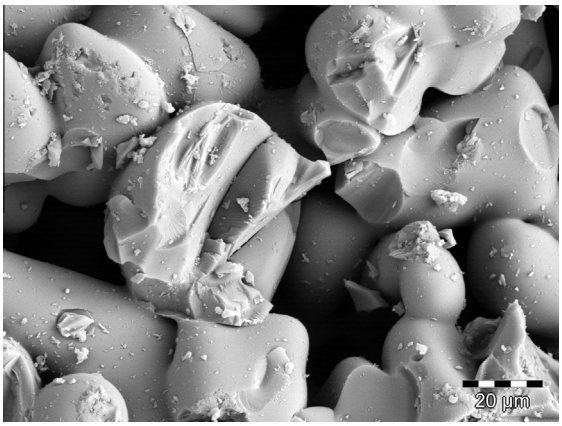

Fig. 1. SEM image for R19 sample.

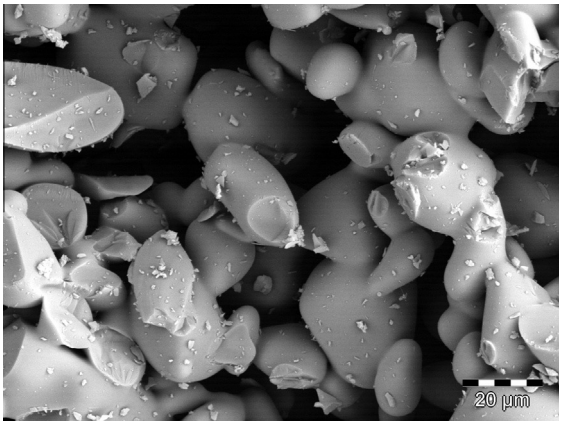

Fig. 2. SEM image for R12 sample.

of 12.3 μm are referred to as R12 or C12. R19T is referred to a rectangular sample with the static pore radius of 19.7 μm that was used for temperature measurements. The morphology of the samples of each pore size group was obtained via Scanning Electron Microscopy (SEM, CamScan Ltd.). The samples were first sputtered with gold to enable the scanning (K550, Emitech, Judges Scientific plc.). SEM images for R19 and R12 samples are presented on Fig. 1 and 2, respectively.

3.1.1. Macroscopic parameters

The open porosity, static pore radius and permeability of the samples were determined under isothermal conditions in experiments with FC-72 liquid, see Table 4. A schematic image of the setup is shown on Fig. 3. The electronic high precision balance (LA310S-0CE, Sartorius) with an accuracy of ±0.0001 g was fixed on a height-adjustable platform and served to measure the sample weight. The sample was located in a closed vessel of 0.095 m diameter partly filled with the experimental liquid. The platform was driven via two stepper motors (VRDM566/50, Berger Lahr/Schneider Electric) with a velocity of 0.38 mm/s to bring the sample into the contact with the liquid surface.

Table 4
Thermophysical properties of FC-72 liquid at 101,325 Pa and 298.15 K.

ρ_L (kg m^{-3})	μ_L (Pa s) 10^{-6}	σ (N m^{-1}) 10^{-3}
1690	709.8	12

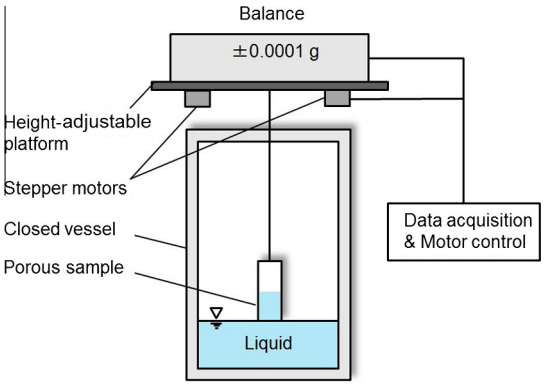

Fig. 3. Schematic image of the setup for isothermal wicking experiments.

The choice of the liquid is explained by the perfect wetting characteristics of FC-72 with most of the materials. Thus, the static contact angle θ with borosilicate glass was taken as zero. Due to its high density FC-72 liquid was also preferable for the static pore radius determination. Some thermophysical properties of FC-72 liquid are summarized in Table 4.

The open porosity characterizes a volume of interconnected pores in a porous structure. This macroscopic parameter was determined using the weight measurements applied to a dry and a saturated porous sample. The obtained mass of the imbibed liquid was used to calculate the open porosity as

$$\phi = \frac{V_{void}}{V_{total}} = \frac{m/\rho_L}{V_{total}}. \quad (15)$$

The static pore radius R_s that indicates a characteristic pore size of a porous structure was determined using the weight of the imbibed liquid corresponding to the equilibrium wicking height h_{eq}

$$P_{eq} = \phi A \rho_L g h_{eq}. \quad (16)$$

The equilibrium wicking height is a maximum achievable wicking height, when the capillary pressure is balanced by the hydrostatic pressure

$$h_{eq} = \frac{2\sigma \cos\theta}{\rho_L g R_s}. \quad (17)$$

This method of the static pore radius determination was also applied by Fries et al. in [10]. In their experiments, Masoodi et al. [35] refer to this value as to the capillary radius. In order to obtain

R_s for the chosen porous structures, the samples of a bigger length should be used. Therefore, rectangular samples were tested that had initially a length of 0.15 m. Due to hardware limitations for experiments with liquid nitrogen the samples were cut to 0.08 m as shown in Table 3.

The permeability K characterizes the ability of a porous structure to conduct a flow through it. To determine this macroscopic parameter, we performed sample weight measurements during the imbibition and calculated the mass of the imbibed liquid. Then the squared mass was plotted versus time for smaller times of the viscous-dominated stage. In this domain governed by the Lucas–Washburn equation the linear regression of the experimental data had a constant slope

$$\frac{m^2}{t} = \frac{4\sigma \cos\theta \rho_L^2 A^2 \phi}{\mu_L} \frac{K}{R_s}. \tag{18}$$

From this slope the relation K/R_s was obtained and, knowing R_s, the permeability was determined. More details on the applied method are provided in [10].

The obtained values of the macroscopic parameters for the experimental samples are summarized in Table 3. The values for each sample are shown with a standard deviation for three test runs. Due to the application of the sample weight measurement technique some corrections were required to account for the buoyancy effect and the surface tension effect on the outer circumference of the samples. More details are provided in Section 4.3, since the sample weight measurement technique was also used for wicking experiments with liquid nitrogen. As opposed to liquid nitrogen experiments, the evaporation of the bulk FC-72 liquid was negligible. However, due to a smaller diameter of the experimental vessel we had to account for a liquid level decrease due to the imbibition of the liquid into the samples. The correction was found to be up to 1.9% for R19 sample, 2.4% for R12 and R12T samples and up to 11.1% for cylindrical samples.

Fig. 4 shows results of isothermal wicking with FC-72 liquid. A theoretical prediction was performed using Eq. (14) and macroscopic parameters from Table 3. Eq. (14). According to [36,37], a porous medium is homogeneous with respect to a given process and a given averaging volume when the effective transport coefficients in the volume-averaged transport equations are independent of position. In our case such transport coefficients are the macroscopic parameters in Eq. (14) that were taken constant for the whole process. A good agreement between the theory and experiment indicates the homogeneity of the porous structures with respect to vertical wicking and the accurate determination of the macroscopic parameters.

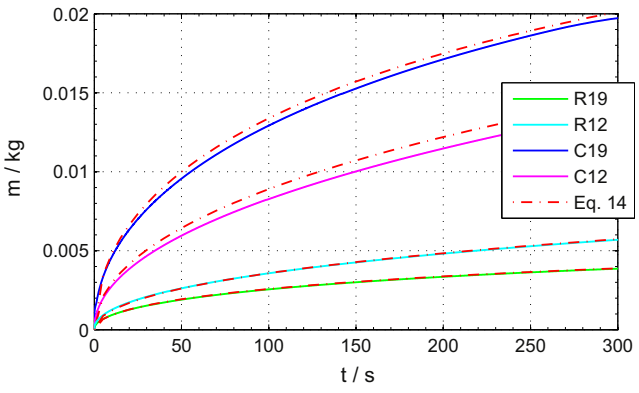

Fig. 4. Isothermal wicking of FC-72 liquid in R19, R12, C19 and C12 samples. The theoretical prediction computed with Eq. (14) is in good agreement with experimental results.

4. Experiment

4.1. Experimental apparatus

A setup was designed to investigate non-isothermal wicking of liquid nitrogen into a superheated porous sample. A schematic image of the setup is depicted on Fig. 5. The stainless steel cylindrical cryostat of 394 mm diameter and 725 mm height and total internal volume of 43 l was facing ambient conditions with $T_a \approx 300$ K at $p_a \approx 101,325$ Pa. The inner tank of the cryostat was evacuated and partly filled with liquid nitrogen at saturation conditions ($T_{LN_2} \approx 77.355$ K at $p_{N_2} \approx p_a$). This ensured having a one-species system (liquid nitrogen in a pure nitrogen vapor) in the cryostat. Thermophysical properties of nitrogen are summarized in Table 6. For better insulation the inner tank was placed in a vacuum casing. The thermally non-insulated lid conducted a heat flux from the ambient at the top of the cryostat. This caused the establishment of a temperature stratification in the nitrogen vapor. Thus, the required non-isothermal conditions for wicking experiments were created.

In order to measure the weight of a porous sample, a weigh cell (WZA1203-N, Sartorius) with an accuracy of ±0.001 g and capacity of 1200 g was placed inside the cryostat. The weigh cell was fixed on a height changeable supporting platform driven via three stepper motors (L3518S1204-T6x1, NanoTec). The motors lifted the platform up and down with a velocity of 2 mm/s. The baffle located at 465 mm from the lid, and the venting line served to protect the weigh cell from over-cooling with nitrogen vapor created during the filling stage. The venting and filling lines were used only during the filling and warming up stages and kept closed during the wicking experiments.

A temperature measurement rod was designed and implemented vertically in the cryostat to determine the temperature distribution in nitrogen vapor and liquid. The measurement rod consisted of an epoxy glass plate and ten temperature sensors allocated along its length. The sensors were silicon diodes DT-670A manufactured by LakeShore for cryogenic conditions. They had an accuracy of ±0.25 K at temperatures from 2 K to 100 K and ± 0.5 K at temperatures from 100 K to 305 K. The thermal dissipation of the sensors was given as 10 μW at 77 K and 5 μW at 305 K. Their response time to a temperature change was specified as 100 ms at

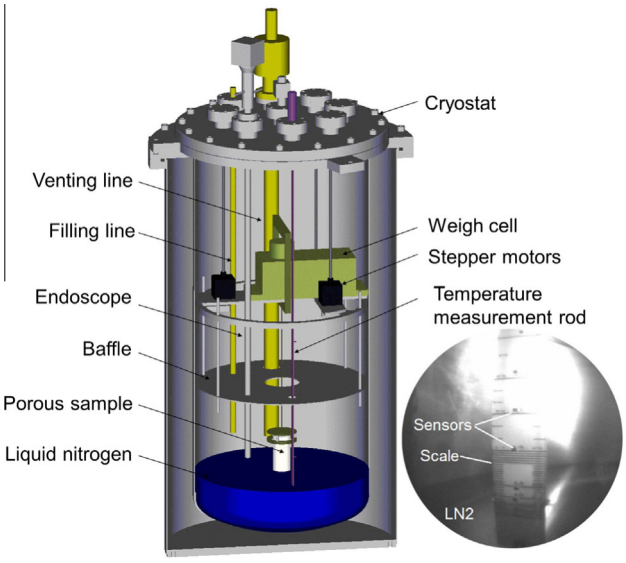

Fig. 5. Schematic image of the setup for non-isothermal wicking experiments with liquid nitrogen.

Table 5
Distances from the lid of the cryostat to the location of the temperature sensors T1 to T10.

Z_1 (m)	Z_2 (m)	Z_3 (m)	Z_4 (m)	Z_5 (m)	Z_6 (m)	Z_7 (m)	Z_8 (m)	Z_9 (m)	Z_{10} (m)
0.595	0.590	0.585	0.580	0.565	0.550	0.535	0.430	0.385	0.340

Table 6
Thermophysical properties of saturated nitrogen (liquid and vapor) at 101,325 Pa and 77.355 K [40]. The static contact angle of liquid nitrogen with borosilicate glass is taken as zero.

Fluid	ρ (kg m^{-3})	μ (Pa s) 10^{-6}	λ (W m^{-1} K^{-1}) 10^{-3}	c_P (J kg^{-1} K^{-1}) 10^{3}	c_V (J kg^{-1} K^{-1}) 10^{3}	σ (N m^{-1}) 10^{-3}	Δh_v (J kg^{-1}) 10^{3}
Liquid	806.08	160.66	144.77	2.0415	1.0841	8.8748	199.18
Vapor	4.6121	5.4440	7.1876	1.1239	0.77128	–	–

77 K and 200 ms at 300 K. The measurement rod was fixed on the lid to ensure the same location of the temperature sensors in the cryostat for each experiment. Distances from the lid to each sensor location are summarized in Table 5. In the vicinity of the liquid level the plate of the measurement rod was scaled. The optical access to the scale, provided via an endoscope, enabled the liquid level determination. A snapshot of the temperature measurement rod obtained with the endoscope is presented on Fig. 5.

A pressure sensor (Sensotec TJE-1256-30) with an accuracy of ±0.2 kPa measured a nitrogen vapor pressure in the ullage of the cryostat.

Weight, temperature and pressure measurements were recorded simultaneously with a sampling rate of 20 Hz.

4.2. Experiment preparation and methodology

The heat flux from the ambient through the lid of the cryostat caused evaporation of nitrogen from the liquid surface. This resulted in a constant liquid level decrease of approximately 3 mm/h. It greatly affected the vapor temperature during the preparation stage that defined the initial temperature distribution for the experiments.

Fig. 6 plots the temperature evolution inside the cryostat during and after the filling with liquid nitrogen. At the end of the filling the sensors T1, T2, T3, T5, T6 and T7 are submerged in the liquid, while the sensors T8, T9 and T10 measure local temperatures in nitrogen vapor. A stable temperature stratification in nitrogen vapor established in approximately 8 h. Due to the liquid level decrease the sensors initially submerged in liquid nitrogen sequentially emerge and start measuring local vapor temperatures. As shown on Fig. 6, after 18 h only sensors T1, T2, T3 and T4 are still in the liquid.

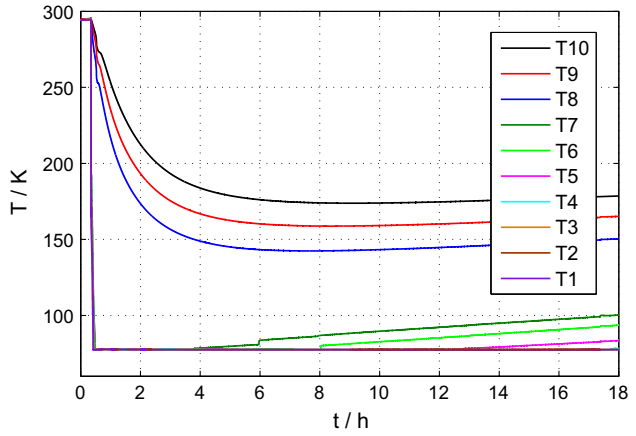

Fig. 6. Temperature evolution inside the cryostat during and after the filling with liquid nitrogen. Sensors T1 to T10 are allocated vertically along the cryostat height. A stable temperature stratification in the nitrogen vapor establishes after approximately 8 h.

To determine the liquid level for each wicking experiment, we ensured first that the liquid level was between two pairs of neighboring temperature sensors T1 and T2 or T3 and T4. The neighboring sensors were spaced out at 5 mm distance from each other, see Table 5. When the liquid level was in between the sensors, the lower sensor showed the liquid nitrogen temperature, while the higher sensor showed the local vapor temperature. The spacing of 5 mm between temperature sensors is sufficient. A closer spacing would not increase the accuracy due to the fact that liquid nitrogen perfectly wets the sensors and forms a meniscus of approximately 1.5 mm height. Using the optical access to the scaled plate provided via the endoscope, it was possible to estimate the liquid level in the cryostat with an uncertainty of 1 mm.

A first wicking experiment for each sample was started when the liquid level was between the sensors T3 and T4 at approximately 582 mm from the lid of the cryostat. In this case the initial sample location was at a maximum distance from the liquid surface. The distance from the sample bottom to the liquid surface was 140 mm for rectangular and 167 mm for cylindrical samples. Due to the heat transfer with the surrounding nitrogen vapor, the sample was superheated with regard to the liquid temperature. To perform the wicking experiment, the sample was driven down and partly submerged into the bulk liquid. The submersion depth was estimated to be between 1 mm and 2 mm. This deviation is explained by the uncertainty in the liquid level determination. The vertical wicking takes place into the unsaturated (not submerged) part of the porous sample. During the imbibition of liquid nitrogen into the porous structure the sample weight increased until a certain value and then stopped. Such an abrupt change of the imbibition behavior corresponds to the moment when the wicking front reached the top of the sample. That was additionally verified by the fact that the final mass of the imbibed liquid nitrogen into each sample corresponds to the porosity value determined in preliminary wicking experiments with FC-72 liquid, see Table 3. Therefore, at the end of each wicking experiment the sample was completely saturated. After that, the sample was driven upwards for approximately 2 mm above the liquid level and kept in this location until the complete evaporation of the imbibed liquid nitrogen. The time to raise the sample from the bulk liquid was always set to 2 s using the motor control system. The actual time needed to detach the sample from the liquid surface was always smaller and was dependent on how deep the sample was submerged. This experiment case is referred to as Superheat 1.

A second wicking experiment was started at approximately 2.5 h from complete evaporation of the imbibed liquid nitrogen out of the sample. At that time the liquid level was between the

sensors T1 and T2 at 592 mm from the lid. The distance from the sample bottom to the liquid surface was only 10 mm for all sample geometries. For that reason the sample superheat obtained through the heat transfer with the surrounding vapor was lower compared to the first experiment (Superheat 1). The sample was driven down to the liquid surface, partly submerged to measure the weight increase until the complete saturation, and then driven for approximately 2 mm above the liquid level to evaporate the imbibed liquid. The methodology for the second wicking experiment was the same as for the first one. This experiment case is referred further to as Superheat 2.

Three test runs were carried out for each experimental case and each porous sample. To guarantee the same temperature distribution for each experiment run, wicking was always initiated at the same liquid level in the cryostat: 582 mm for the first wicking experiment and 592 mm for the second (measured from the lid).

In addition, experiments were conducted to trace the sample temperature evolution. After the macroscopic parameters were determined for R12T, two elliptical holes of 2 mm and 3 mm diameters and 6 mm depth were drilled on its lateral side. The holes were located at 10 mm and 60 mm distance from the sample bottom. One temperature sensor (silicon diodes DT-670A, LakeShore) was embedded inside each hole. Simultaneous sample weight and temperature measurements were performed in Superheat 1 and 2 experiment cases.

4.3. Correction of sample weight measurements

To initiate wicking, a porous sample was partly submerged into the bulk liquid. That induced some sample weight decrease due to buoyancy. Taking into account the uncertainty in the liquid level determination, a calculation of the buoyancy force would not be accurate. In Section 4.2 we also mentioned that the heat flux from the ambient caused the evaporation of the bulk liquid in the cryostat. The corresponding liquid level decrease of 3 mm/h influenced the sample weight measurements during the imbibition. Using the liquid level decrease rate, we corrected the measurement data to eliminate the sample weight changes.

In addition to that, an outer meniscus forms at the sample perimeter upon contact of the sample with the liquid surface. This effect leads to some weight increase and is known as the Wilhelmy force. For non-porous samples it can be estimated using the Wilhelmy plate method [38,39]. Nevertheless, due to the porous structure of the experimental samples the accurate determination of the Wilhelmy force was not possible.

The sample weight changes due to the buoyancy force, the Wilhelmy force and early wicking occur almost simultaneously and are difficult to separate. However, if the total weight change caused by the buoyancy force and the Wilhelmy force is constant, it can be found subtracting the final weight of a completely saturated but still partly submerged sample from the actual weight of the saturated sample. The actual weight of the saturated sample should be measured immediately when the sample is detached from the liquid surface, and before the evaporation reduces the weight. In such a way, the results of the sample weight measurements were corrected to account for the buoyancy and the surface tension effects. The total correction was found to be up to 1.3% for R19 sample, 1.7% for R12 and R12T samples and up to 3.7% for cylindrical samples.

5. Results and discussion

This section is divided into three parts. In the first part, the experiment environment is analyzed using the nitrogen vapor temperature evolution during the imbibition and shortly before and after that. The second part presents results of simultaneous sample weight and temperature measurements with four identified experiment stages. In the third part, the influence of various porous structures, sample geometries and superheats on the mass of the imbibed liquid nitrogen are compared to theoretical predictions.

5.1. Temperature evolution of nitrogen vapor

Fig. 7 depicts the temperature distribution in the cryostat before the first (Superheat 1) and second wicking experiment (Superheat 2). The circles in Fig. 7 indicate readings of the temperature sensors plotted versus their locations in the cryostat at the moment when the sample was driven to the liquid surface. The initial sample position for rectangular (R) and cylindrical samples (C) is shown via arrows and dotted lines. The dot-dashed lines display the liquid level in the cryostat. For Superheat 1 case the initial sample position corresponds to a maximum achievable distance from the sample to the liquid surface. For Superheat 2 the sample is at a minimum distance.

Linear temperature gradients established in a stratified nitrogen vapor environment below and above the baffle. Above the baffle the gradient and absolute temperatures were of interest for Superheat 1, since it reflected vapor temperature distribution at the initial sample position and defined the superheat. The gradient and absolute temperatures below the baffle were of interest for Superheat 2. The average sample superheat values were higher at Superheat 1, however, temperature gradients for this case were smaller compared to Superheat 2. Assuming the same temperature distribution in the sample as in the surrounding vapor, the temperatures at the sample top and bottom were estimated. The obtained values are summarized in Table 7.

Furthermore, all the sensors display higher vapor temperatures in Superheat 2 case, see Fig. 7. This is substantiated by the liquid level decrease and the movement of the supporting platform with the weigh cell and stepper motors from the warmer region close to the lid to the colder region of the baffle location. The influence of the platform movement is most pronounced for T8, T9 and T10 sensors allocated in the upper part of the cryostat.

T1, T2, T3, T4, T5, T6 and T7 sensors measure vapor and liquid temperatures at the wicking sample location. Fig. 8 demonstrates their temperature evolutions for each experiment. The first vertical line on each figure indicates the beginning of the wicking process. Particularly, $t = 0$ here and on all the further figures corresponds to the stop of the sample movement towards the bulk liquid. At that moment the sample was submerged at 1–2 mm and wicking into the upper not-submerged part of the sample occurred. The second vertical line depicts the moment of full saturation of the sample. The time period between these lines corresponds to the wicking time.

The vapor temperature changes during the experiments. It increases from the moment of the sample movement, reaches a maximum value during the wicking process and then again decreases to an approximately initial value. Such a behavior is caused by the heat transfer between the sample and the surrounding vapor. A vapor temperature increase is most pronounced for Superheat 1 case due to higher values of the sample superheat. During the imbibition of liquid nitrogen the sample structure cools down and starts cooling the surrounding vapor. That is clearly seen for both experiment cases. One also notices that heating and cooling of the surrounding vapor are most pronounced for cylindrical samples that had larger mass and surface area per a sample length for the heat transfer.

Fig. 8 also shows that for each sample the wicking time was longer in the experiments with Superheat 1 than with Superheat 2. This indicates that higher superheats cause a wicking time

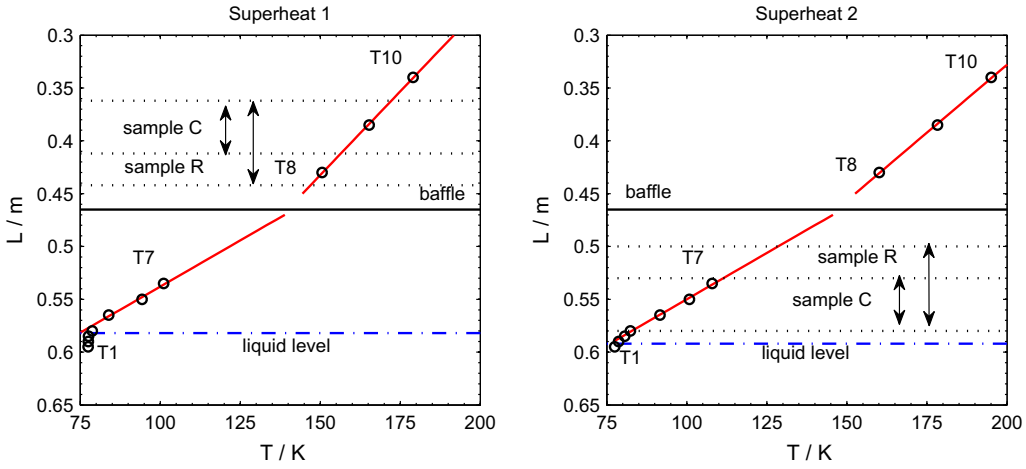

Fig. 7. Temperature distribution in the cryostat before the first (Superheat 1) and second wicking experiment (Superheat 2). It illustrates the establishment of linear temperature gradients in a stratified nitrogen vapor environment below and above the baffle. The initial sample position for rectangular (R) and cylindrical samples (C) is shown via arrows and dotted lines. The liquid level displayed by the dot-dashed lines was slightly lower for Superheat 2 case resulting in higher temperature values of sensors T1 to T10.

Table 7
Initial linear temperature gradient in a stratified nitrogen vapor environment along the sample length and calculated sample temperature at the bottom T_0 and top T_{SL}.

Sample	T_0 (K)	T_{SL} (K)	$\Delta T_S/L$ (K m^{-1})
Superheat 1			
R19	146.9 ± 0.8	172.3 ± 0.8	316.9 ± 0.7
R12	146.9 ± 0.3	171.9 ± 0.3	313.5 ± 2.0
R12T	147.2 ± 0.3	172.6 ± 0.2	317.3 ± 1.4
C19	154.5 ± 1.2	170.6 ± 1.2	323.4 ± 1.7
C12	155.9 ± 2.0	172.0 ± 1.9	321.3 ± 2.1
Superheat 2			
R19	82.3 ± 0.3	127.9 ± 0.6	571.1 ± 4.2
R12	82.6 ± 0.3	127.7 ± 0.4	564.5 ± 1.3
R12T	83.0 ± 0.6	128.2 ± 0.4	565.7 ± 2.3
C19	82.1 ± 0.2	110.8 ± 0.5	573.9 ± 6.8
C12	81.6 ± 0.3	110.1 ± 0.4	569.6 ± 1.0

increase. Comparing results for samples of identical geometry, one also observes that the wicking time is longer for samples of smaller permeability. For example, C12 sample needed approximately 130 s to get saturated with liquid nitrogen in Superheat 2 case, while C19 sample of higher permeability needed only 80 s. The same trend holds for Superheat 1 runs.

5.2. Imbibed liquid mass and sample temperature

This part presents results of simultaneous sample weight and temperature measurements during the imbibition of liquid nitrogen in R12T sample. Wicking experiments referred in previous sections as Superheat 1 and Superheat 2 were performed. The mass of the imbibed liquid was calculated using dry sample weight measurements and sample weight measurements during the imbibition.

Fig. 9 demonstrates the mass increase of the imbibed liquid nitrogen and simultaneous temperature evolution obtained with T11 and T12 sensors. These sensors were embedded into two holes along the sample length. More details on the sensor allocation are provided in Section 4. The vertical lines on Fig. 9 separate different stages of the experiment.

During the stage I the sample was moved from its initial position to the liquid surface. The sample movement caused some sample weight perturbations recorded by the weigh cell and corresponded to the mass perturbations shown on Fig. 9. The perturbation time was smaller for Superheat 2 when the sample was moved at a smaller distance. Fig. 9 also shows that for Superheat 1 case the heat transfer between the sample and surrounding vapor led to a significant sample temperature decrease. This is demonstrated by the change of T11 and T12 sensors readings from 154.3 K and 167.6 K at the initial sample position to approximately 125.9 K and 148.2 K, respectively, at the wicking start. In the case of Superheat 2 the sample movement caused a temperature change from 93.3 K and 114.9 K to approximately 92.1 K and 114.4 K for T11 and T12 sensors, respectively.

The stage II corresponds to the wicking process. The mass of the imbibed liquid increases in time. When the wicking front passes through the sensor location, the sensor reading decreases abruptly. Thus, the abrupt temperature decrease is a wicking front indicator. A smooth temperature decrease can be also seen for T12 sensor before the abrupt one. This is contributed by the heat conduction in the solid structure of the sample and the heat transfer between the solid structure and newly created vapor.

The constant liquid mass and sample temperature during the stage III on Fig. 9 indicate the saturation of the sample with liquid nitrogen. The temperature of the saturated sample is approximately 80 K that exceeds the liquid nitrogen temperature (77.355 K). Such a difference might be due to some imperfections in fixing of T11 and T12 sensors on the porous surface inside the holes. In fact, the sensors might partly measure the vapor temperature. Another possible explanation could be a creation of vapor pockets in the porous structure during the imbibition.

The stage IV starts at the moment when the sample is detached from the liquid surface. The mass decrease on Fig. 9 indicates evaporation of the imbibed liquid out of the sample. Due to the heat transfer with the surrounding vapor the sample temperature increases.

5.3. Imbibed liquid mass at various porous structures, sample geometries and superheats

In this part, the experiment stage II that directly relates to the imbibition is under investigation for Superheat 1 and 2 cases. The sample weight measurements were conducted during wicking of liquid nitrogen into R19, R12, C19 and C12 samples to obtain the mass of the imbibed liquid. The measurements were corrected in accordance with the argumentation provided in Section 4.3.

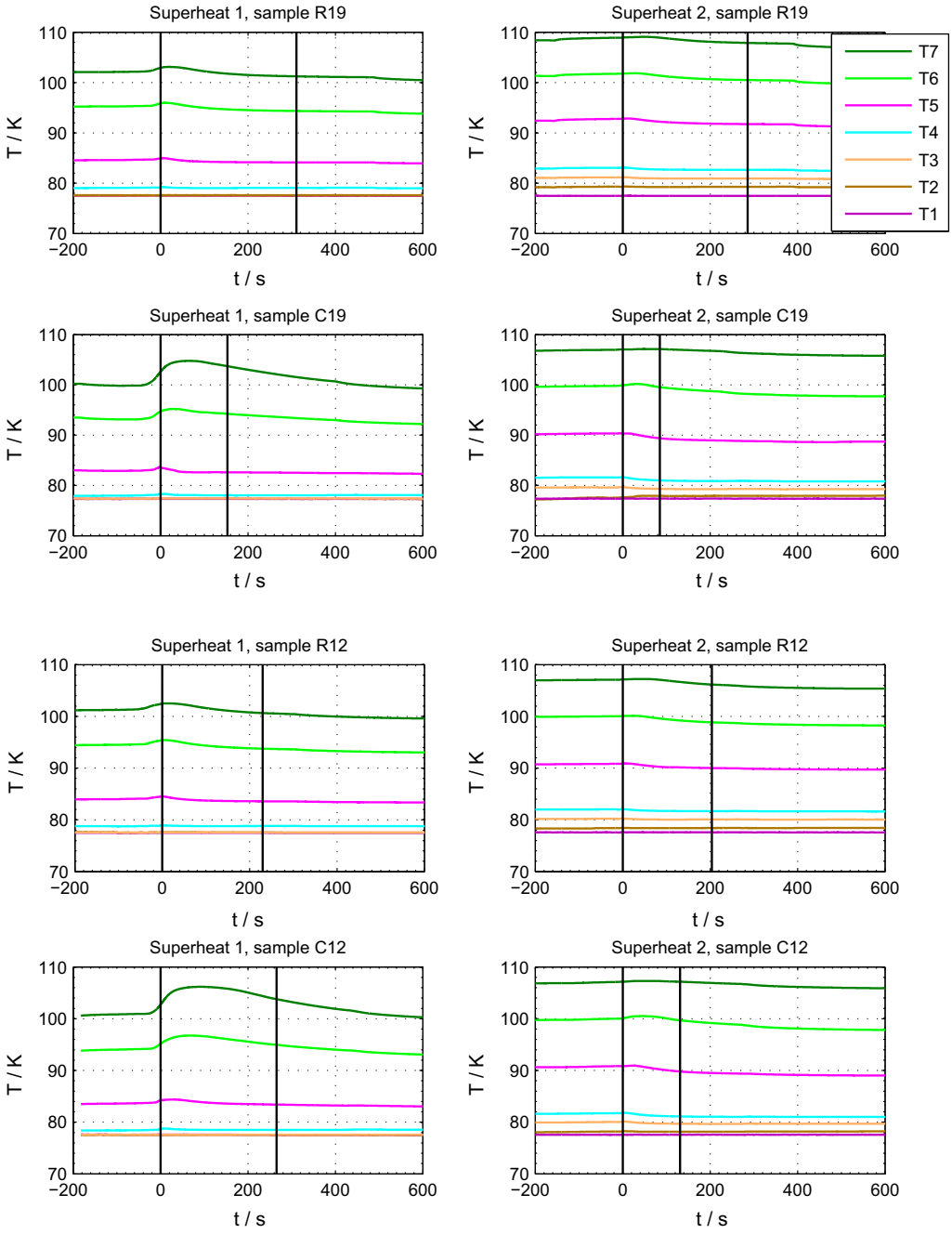

Fig. 8. Vapor temperature evolution during the imbibition of liquid nitrogen into superheated porous samples.

The theoretical prediction was performed using the proposed model with Eq. (13). The model predicts the imbibition in form of the wicking height increase in time. In order to compare it with experimental results, the wicking height was recalculated into the wicking mass using

$$m(t) = \rho_L \phi A h(t). \tag{19}$$

In addition, the theoretical prediction for the isothermal case (no sample superheat) at saturation temperature of liquid nitrogen was performed with Eq. (14).

The parameters of Eq. (13) and (14) were computed using thermophysical properties of liquid nitrogen at saturation temperature and borosilicate glass, sample geometrical characteristics and macroscopic parameters and sample temperatures. As shown in Section 5.2, in Superheat 1 case the sample temperature decreases from its initial value during the sample movement to the liquid surface. Results of R12T sample temperature measurements were used to calculate sample temperatures at the wicking start. 122 K and 157 K were obtained for rectangular samples at the bottom and top, respectively, and 129 K and 151 K for cylindrical samples. In case of Superheat 2 no significant sample temperature decrease was observed due to the sample movement, therefore, the temperatures from Table 7 were as the sample temperature.

We noticed, however, some deviations of the sample temperature measured by the sensors T11 and T12 from the corresponding vapor temperatures. Fig. 10 shows sample and vapor temperatures before the sample R12T was moved to the liquid surface in Superheat 2 case. The sample top and bottom temperatures deviate up to 5 K, comparing the vapor and sample temperature measurement values. This might be stipulated by the fact that the solid porous

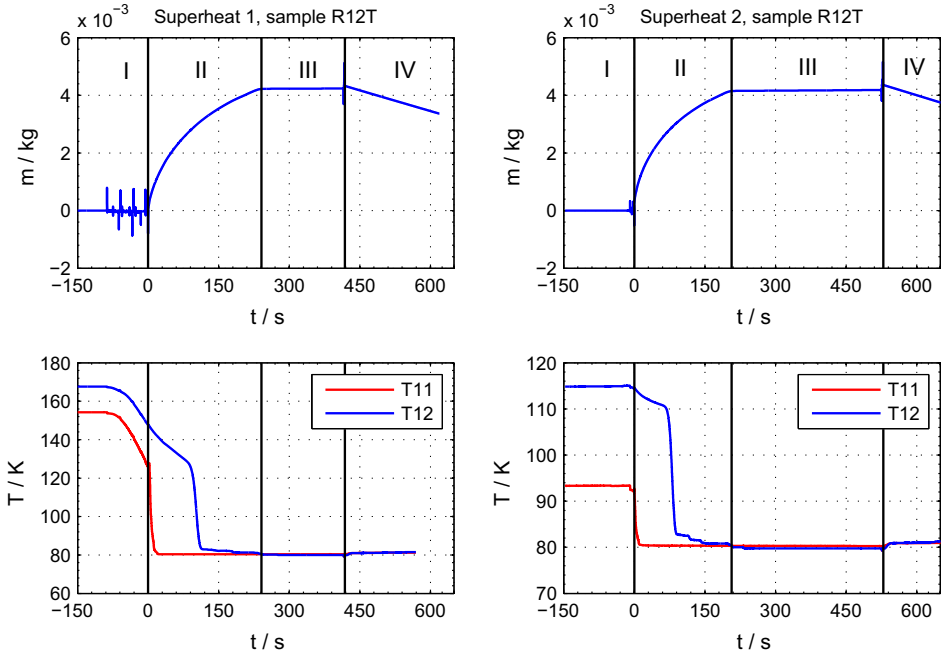

Fig. 9. The mass of the imbibed liquid and sample temperature evolution obtained with T11 and T12 sensors during the imbibition of liquid nitrogen into superheated porous sample R12T. The vertical lines separate different stages of the experiment.

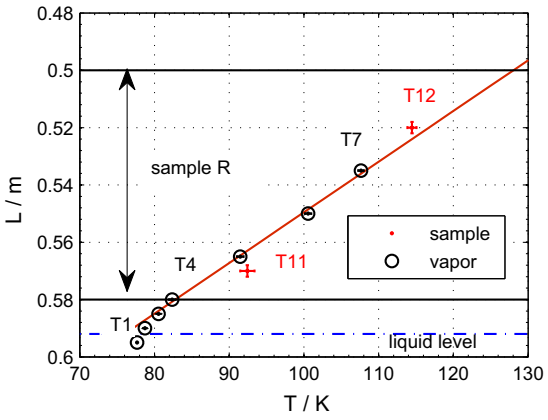

Fig. 10. The sample (T11 and T12) and the vapor (T1 to T7) temperatures before the second wicking experiment (Superheat 2) for the sample R12T. Sample temperature deviates from the corresponding vapor temperature. The values are shown with a standard deviation for three experiment runs. The sample position is shown via arrows and solid black lines. The liquid level is displayed by a dot-dashed blue line. (For interpretation of the references to color in this figure legend, the reader is referred to the web version of this article.)

structure with the vapor in its pores was located in the stratified bulk vapor environment that was constantly influenced by the evaporation of the bulk liquid. Therefore, we took an uncertainty of ±5 K in the sample temperature determination and accounted for this in an error analysis for the theoretical model prediction, provided in Section 5.4.

Schnelle et al. [42] deduced a polynomial equation that describes the temperature dependence of the specific heat capacity of borosilicate glass 3.3 in the range from 48.2 K to 320 K

$$c_S(T) = \exp\left[\sum a_i (\ln T)^i\right], \tag{20}$$

where a_i are empirical coefficients. Eq. (20) was used to calculate the specific heat capacity at average sample temperatures. The parameter values for all the samples are summarized in Table 8.

Table 8
List of the parameters of Eqs. (13) and (14).

Sample	ϵ (–)	b (s m^{-2}) 10^4	c (m^{-1})	n_1 (–)	n_2 (m^{-1})
Superheat 1					
R19	1.50	4.70	8.76	0.26	1.81
R12	1.27	5.38	5.47	0.26	1.80
C19	1.89	4.92	8.76	0.30	1.90
C12	2.23	10.17	5.47	0.30	1.89
Superheat 2					
R19	1.50	4.70	8.76	0.022	2.49
R12	1.27	5.38	5.47	0.023	2.46
C19	1.89	4.92	8.76	0.019	2.27
C12	2.23	10.17	5.47	0.017	2.24

The parameters ϵ and b in Table 8 are different for the samples due to the fact that they include porosity and permeability values, which depend on a porous structure of each sample. The parameter c is equal for the samples of similar characteristic pore size. However, at both superheats the parameters n_1 and n_2, which include sample and liquid temperatures, deviate only slightly for samples of identical geometry. This indicates that tests were conducted under comparable conditions (with the same fluid and at approximately equal temperatures). The higher sample superheat, the bigger n_1 is. The parameter n_2 in its turn is higher for higher temperature gradients in porous structures.

Fig. 11 shows experimental results and theoretical predictions for rectangular samples R19 and R12. A qualitative agreement between the theory and experiment was reached for both samples. Moreover, the relative decrease of the imbibition rate between two experimental curves at lower and higher sample superheats is in good quantitative agreement with predictions via Eq. (13). The experiment and theory also evidence that even for high sample superheat (122 K at the sample bottom) the results deviate only slightly from the results for much lower superheat (82 K at the sample bottom). Therefore, the liquid loss due to evaporation caused by the heat transfer between liquid nitrogen and superheated sample does not lead to a considerable decrease of the imbibition rate.

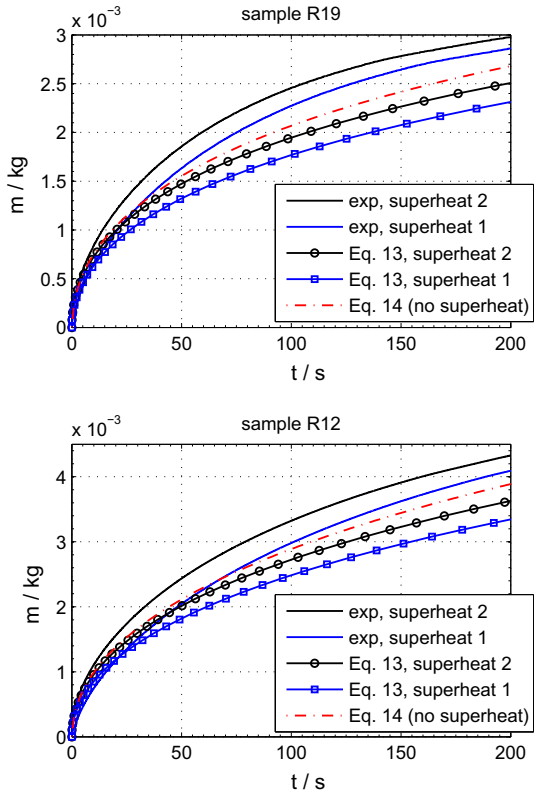

Fig. 11. The mass of the imbibed liquid nitrogen during wicking in superheated porous samples R19 and R12. For both samples the relative decrease of the imbibition rate between two experimental curves at lower (2) and higher (1) sample superheats is in good agreement with predictions via Eq. (13). High sample superheat does not lead to a considerable decrease of the imbibition rate.

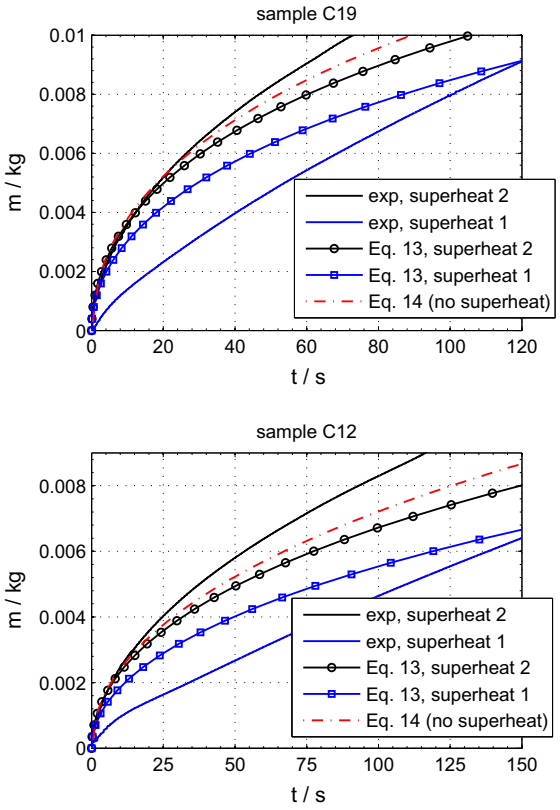

Fig. 12. The mass of the imbibed liquid nitrogen into superheated porous samples C19 and C12. The vapor flow created due to evaporation in Superheat 1 case significantly slows down the imbibition rate and changes the wicking behavior. Eq. (13) neglecting the vapor flow impact provides a qualitative theoretical description only at smaller Superheat 2.

The predictions with Eqs. (13) and (14) underestimate the imbibition rate. Such a result might be connected to the assumptions made for the model derivation. The heat needed to cool down the superheated solid structure above the wicking front was assumed to be entirely taken from the latent heat of evaporation of the liquid at saturation temperature. In fact, in the vicinity of the liquid–vapor interface heat transfer occurs between the rising liquid, the superheated porous structure, the newly created cold vapor and the superheated vapor initially contained in the structure. As a result the actual liquid–vapor interface temperature in the pores might differ from 77.355 K taken for calculations. Correspondingly, the thermophysical properties of the liquid taken for calculations will be affected. Especially, one should note here such a temperature dependent property as the surface tension that defines the capillary pressure for the imbibition. Hartwig et al. [18,43,44] observed the effect of evaporation and condensation measuring the liquid nitrogen, oxygen and methane bubble point pressures for steel meshes using non-condensable and autogenous pressurization schemes. The authors noted significant differences between the bulk vapor and liquid temperatures and the corresponding screen side temperatures. The evaporation in experiments with a non-condensable pressurization led to the decrease of the interfacial temperature and, thus, to the increase of the local surface tension. The condensation in experiments with an autogenous pressurization caused the increase of the interfacial temperature and the decrease of the local surface tension.

Fig. 12 plots experimental data and theoretical predictions at two sample superheats for cylindrical samples C19 and C12. The theory describes results qualitatively for smaller Superheat 2. Meanwhile, results for higher Superheat 1 drastically deviate from the model predictions. Previous examination revealed that the liquid loss due to evaporation could not cause such deviations. Thereby, such a behavior might be only stimulated by the vapor flow created due to evaporation. This vapor builds up an additional pressure in the pores above the rising liquid which slows down the imbibition rate. Due to relatively small cross-sections of R19 and R12 samples, the vapor could easily escape from the structures through their lateral sides, thus, its influence was negligible for wicking. However, in C19 and C12 samples the rising liquid pushes a larger amount of newly created vapor out of the structures along more complex and long trajectories. Moreover, the higher sample superheat, the more vapor is created. Therefore, the vapor flow effect is most pronounced for highly superheated samples of large cross-sections and may greatly slow down the imbibition rate. That is in conformity with results for C19 and C12 samples with Superheat 1.

5.4. Error analysis for theoretical model prediction

We provide an error analysis of the theoretical model prediction with Eq. (13). The model parameters contain macroscopic parameters of the samples and sample temperatures that are the error sources for the prediction, see Table 1. The deviations in the determination of the macroscopic parameters are presented Table 3. In consequence with the observed discrepancy of the results of sample and vapor temperature measurements, we assume an error of ±5 K in the sample temperatures determination. Table 9 summarizes results of the estimation of relative errors for determined parameters of Eq. (13) and relative errors for the model prediction. We noticed a large discrepancy in the determination of n_1 for

Table 9
List of relative errors for determined parameters of Eq. (13) and relative errors for the model prediction.

Sample	$\delta\epsilon$ (%)	δb (%)	δc (%)	δn_1 (%)	δn_2 (%)	$\delta t(h)$ (%)	$\delta t(m)$ (%)
Superheat 1							
R19	8.33	6.69	2.03	11.2	28.9	9.26	12.7
R12	8.12	6.78	2.44	11.2	29.7	8.61	11.4
C19	8.79	11.2	2.03	8.67	27.5	12.6	14.0
C12	9.35	13.6	2.44	8.67	28.0	15.1	16.5
Superheat 2							
R19	8.33	6.69	2.03	101	20.6	8.60	12.2
R12	8.12	6.78	2.44	95.3	19.7	7.96	11.0
C19	8.79	11.2	2.03	105	21.0	12.0	13.4
C12	9.35	13.6	2.44	118	20.4	14.5	16.2

Superheat 2 case due to errors in the sample temperature determination. However, the absolute values of n_1 for Superheat 2 were relatively small compared to n_2/c and, therefore, only slightly influenced the final results. The relative errors for the model prediction of the mass of the imbibed liquid nitrogen versus time were estimated to be up to 12.7% for rectangular and up to 16.5% for cylindrical samples, see Table 9.

5.5. Comparison to historical results

In our experiments we characterized the wicking rate of liquid nitrogen measuring the weight of the imbibed liquid into porous structures of a different pore size. Unfortunately, no reference data for the wicking rate of liquid nitrogen was found in literature. However, Zhang et al. [11] performed experiments demonstrating the presence of liquid nitrogen in a metallic mesh due to wicking. The authors also reported that the height of the liquid column due to capillary effects is often used as a metric for wicking performance. The maximum height of the liquid column due to wicking, or the equilibrium wicking height, characterizes a balance between the capillary pressure and the hydrostatic pressure. We also introduced it in Eq. (17). Zhang et al. [11] showed a prediction of the equilibrium wicking height for different effective radii of a porous structure and reported their experimentally determined wicking height for liquid nitrogen. The authors demonstrated a wicking height of 60 mm for a mesh structure with a pore size of approximately 5 μm. We achieved a wicking height of 80 mm for sintered glass frits structures with a pore size of approximately 39.4 μm and 24.6 μm. The results are plotted together on Fig. 13. It should

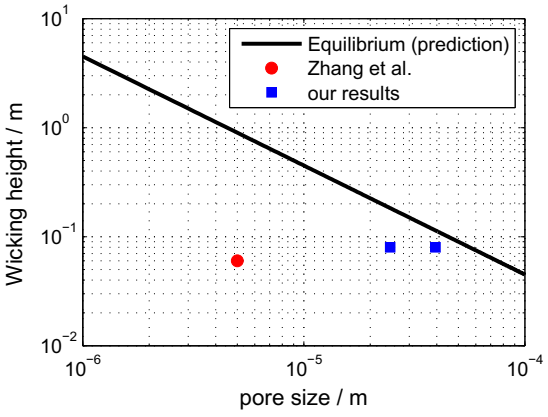

Fig. 13. The wicking height of liquid nitrogen at different pore sizes. The equilibrium wicking height is predicted using Eq. (17) and properties of liquid nitrogen at 101,325 Pa and 77.355 K. The static contact angle is taken as zero. A red circle corresponds to a wicking height reported by Zhang et al. [11], blue squares correspond to our results. (For interpretation of the references to color in this figure legend, the reader is referred to the web version of this article.)

be mentioned that our values and the values reported by Zhang et al. [11] are not claimed to be the equilibrium wicking height. However, these are the first reported values of the wicking height of liquid nitrogen.

6. Conclusion

Wicking of liquid nitrogen at saturation temperature into vertical superheated porous structures was studied. Experiments were performed in a one-species system under pre-defined non-isothermal conditions to determine the mass of the imbibed liquid nitrogen measuring a sample weight increase during the imbibition. The setup configuration enabled to define a sample superheat by its initial position in a stratified vapor environment inside the cryostat. To the author's extent of knowledge these are the first wicking experiments performed with a cryogenic fluid subjected to evaporation using the weight–time measurement technique.

Two experimental cases with regard to a sample superheat value were examined. The vapor temperature distribution with established linear gradients in the initial and the wicking sample location was determined in the cryostat. The vapor temperature evolution demonstrated the interaction of superheated porous structures with the surrounding vapor. Simultaneous sample weight and temperature measurements were conducted. Four experiment stages were identified in accordance with the weight and temperature responses. During the imbibition stage these responses indicated the wicking front velocity. The temperature decrease due to the heat conduction within the solid structure, and heat transfer between the solid structure and surrounding vapor was observed.

The impact of the porous sample superheat, structural and geometrical characteristics on the imbibition rate was investigated. A one-dimensional macroscopic model is proposed to evaluate the imbibition rate. Experimental and theoretical results are in a qualitative agreement and revealed that the liquid loss due to evaporation caused by the heat transfer between liquid nitrogen and superheated sample does not lead to a significant decrease of the imbibition rate. Only a slight decrease of the imbibition rate was observed for highly superheated samples of small cross-sections. In this case a good quantitative agreement between the experiment and theory was found for the relative decrease of the imbibition rate at two sample superheats. However, results of wicking with samples of larger cross-sections showed that the imbibition rate can be greatly affected by the vapor flow. The vapor created above the wicking front due to the heat transfer of the liquid with superheated porous structure counteracts the wicking front propagation and significantly slows down the process. Due to a larger amount of the created vapor and a more complex trajectory to escape of the porous structure, this effect is most pronounced for highly superheated samples of large cross-sections.

In our experiment with liquid nitrogen we achieved a wicking height of 80 mm for sintered glass frits structures with a pore size of approximately 39.4 μm and 24.6 μm. Along with the data presented by Zhang et al. [11] these values are the first reported values of the liquid nitrogen wicking height.

Acknowledgements

This work was supported by the German Research Foundation (DFG) within the Research Training Group GRK 1860 "Micro-, meso- and macroporous nonmetallic Materials: Fundamentals and Applications" (MIMENIMA). The authors acknowledge gratefully Peter Prengel, Frank Ciecior and Holger Faust for their effort in preparing and performing the experiments.

Appendix A

Integrating Eq. (12), one obtains

$$t(h) = \int \frac{b(1+\epsilon(n_1+n_2h))h}{1-ch}\mathrm{d}h = b(1+\epsilon n_1)\underbrace{\int \frac{h\mathrm{d}h}{1-ch}}_{1} + b\epsilon n_2 \underbrace{\int \frac{h^2}{1-ch}\mathrm{d}h}_{2}. \quad (21)$$

Solving the integral 1 of Eq. (21)

$$\int \frac{h\mathrm{d}h}{1-ch} = -\frac{1}{c}\int \frac{-ch\mathrm{d}h}{1-ch} = -\frac{1}{c}\int \frac{1-ch-1}{1-ch}\mathrm{d}h = -\frac{1}{c}\int\left(1-\frac{1}{1-ch}\right)\mathrm{d}h = -\frac{1}{c}\left[h+\frac{1}{c}\ln(1-ch)\right], \quad (22)$$

and the integral 2 of Eq. (21)

$$\begin{aligned}\int \frac{h^2}{1-ch}\mathrm{d}h &= -\frac{1}{c^2}\int \frac{-c^2h^2}{1-ch}\mathrm{d}h = -\frac{1}{c^2}\int \frac{1-c^2h^2-1}{1-ch}\mathrm{d}h \\ &= -\frac{1}{c^2}\int\left[\frac{(1-ch)(1+ch)}{1-ch}-\frac{1}{1-ch}\right]\mathrm{d}h \\ &= -\frac{1}{c^2}\int\left(1+ch-\frac{1}{1-ch}\right)\mathrm{d}h \\ &= -\frac{1}{c^2}\left[h+\frac{ch^2}{2}+\frac{1}{c}\ln(1-ch)\right], \end{aligned} \quad (23)$$

and substituting the solutions to Eq. (21), one obtains

$$\begin{aligned} t(h) &= -\frac{1}{c}\left[h+\frac{1}{c}\ln(1-ch)\right]b(1+\epsilon n_1) \\ &\quad -\frac{b\epsilon n_2}{c^2}\left[h+\frac{ch^2}{2}+\frac{1}{c}\ln(1-ch)\right] \\ &= -\frac{b}{c}\left[(1+\epsilon n_1)h+\frac{1}{c}(1+\epsilon n_1)\ln(1-ch)\right] \\ &\quad -\frac{b}{c}\left[\frac{\epsilon n_2}{c}h+\frac{\epsilon n_2h^2}{2}+\frac{\epsilon n_2}{c^2}\ln(1-ch)\right] \\ &= -\frac{b}{c}\left[\left(1+\epsilon\left(n_1+\frac{n_2}{c}\right)\right)h\right] \\ &\quad -\frac{b}{c}\left[\left(1+\epsilon\left(n_1+\frac{n_2}{c}\right)\right)\frac{1}{c}\ln(1-ch)\right]-\frac{b}{c}\frac{\epsilon n_2h^2}{2} \\ &= -\frac{b\epsilon n_2}{2c}h^2-\frac{b}{c}\left(1+\epsilon\left(n_1+\frac{n_2}{c}\right)\right)\left(h+\frac{1}{c}\ln(1-ch)\right). \end{aligned} \quad (24)$$

References

[1] Jaekle DE. Propellant management device conceptual design and analysis: galleries. In: AIAA-97-2811.
[2] Wollen M, Merino F, Schuster J, Newton C. Cryogenic propellant management device: conceptual design study. In: NASA/CR-010-216777.
[3] Chato DJ, Kudlac MT. Screen channel liquid acquisition devices for cryogenic propellants. In: AIAA-2002-3983.
[4] Darr S, Hartwig J. Optimal liquid acquisition device screen weave for a liquid hydrogen fuel depot. Int J Hydrogen Energy 2014;39:4356–66.
[5] Hartwig J, Darr S. Influential factors for liquid acquisition device screen selection for cryogenic propulsion systems. Appl Therm Eng 2014;66:548–62.
[6] Jurns JM, Hartwig JW. Liquid oxygen liquid acquisition device bubble point tests with high pressure lox at elevated temperatures. Cryogenics 2012;52:283–9.
[7] Behruzi P, Klatte J, Netter G. Passive phase separation in cryogenic upper stage tanks. In: Proceeding of 49th AIAA/ASME/SAE/ASEE Joint Propulsion Conference, San Jose, USA.
[8] Conrath M, Smiyukha Y, Fuhrmann E, Dreyer M. Double porous screen element for gas-liquid phase separation. Int J Multiphase Flow 2013;50:1–15.
[9] E.P. Symons. Wicking of liquids in screens. NASA TN D-7657, 1974.
[10] Fries N, Odic K, Conrath M, Dreyer M. The effect of evaporation on the wicking of liquids into a metallic weave. J Colloid Interface Sci 2008;321:118–29.
[11] Zhang T, deBock P, Stautner EW, Deng T, Immer C. Demonstration of liquid nitrogen wicking using a multi-layer metallic wire cloth laminate. Cryogenics 2012;52:301–5.
[12] Choi SW, Lee WI, Kim HS. Analysis of flow characteristics of cryogenic liquid in porous media. Int J Heat Mass Transfer 2015;87:161–83.
[13] Vanderlaan MH, Van Sciver SW. He II heat transfer through random packed spheres: pressure drop. Cryogenics 2014;63:37–42.
[14] Vanderlaan MH, Van Sciver SW. Steady state He II heat transfer through random packed spheres. Cryogenics 2013;57:166–72.
[15] Allain H, Baudouy B, Quintard M, Prat M. Experimental investigation of heat transfer through porous media in superfluid helium. Cryogenics 2015;66:53–62.
[16] Hartwig J, Mann Jr JA, Darr SR. Parametric analysis of the liquid hydrogen and nitrogen bubble point pressure for cryogenic liquid acquisition devices. Cryogenics 2014;63:25–36.
[17] Hartwig J, Chato D, McQuillen J. Screen channel LAD bubble point tests in liquid hydrogen. Int J Hydrogen Energy 2013;39(2):853–61.
[18] Hartwig J, McQuillen J, Jurns J. Screen channel liquid-acquisition-device bubble point tests in liquid oxygen. J Thermophys Heat Transfer 2015;29(2):353–63.
[19] Ranjan R, Murthy JY, Garimella SV. A microscale model for thin-film evaporation in capillary wick structures. J Heat Mass Transfer 2011;54:169–79.
[20] Bodla KK, Murthy JY, Garimella SV. Evaporation analysis in sintered wick microstructures. J Heat Mass Transfer 2013;61:729–41.
[21] Xuan Y, Zhao K, Li Q. Investigation on heat and mass transfer in a evaporator of a capillary-pumped loop with the lattice Boltzmann method: pore scale simulation. Transp Porous Media 2011;89(3):337–55.
[22] Prat M. Pore network models for the study of transfers in the porous wick of loop heat pipes. Heat Pipe Sci Technol 2010;1(2):129–49.
[23] Mottet L, Coquard T, Prat M. Three dimensional liquid and vapour distribution in the wick of capillary evaporators. J Heat Mass Transfer 2015;83:636–51.
[24] Fries N, Dreyer M. An analytic solution of capillary rise restrained by gravity. J Colloid Interface Sci 2008;320:259–63.
[25] Fries N, Dreyer M. Dimensionless scaling methods for capillary rise. J Colloid Interface Sci 2009;338:514–8.
[26] Washburn EW. The dynamics of capillary flow. Phys Rev 1921;17(3):273–83.
[27] Lucas R. Ueber das Zeitgesetz des kapillaren Aufstiegs von Fluessigkeiten. Kolloid-Z 1918;23:15–22.
[28] Stange M, Dreyer M, Rath H. Capillary driven flow in circular cylindrical tubes. Phys Fluids 2003;15:2587–601.
[29] Fries N, Dreyer M. The transition from inertial to viscous flow in capillary rise. J Colloid Interface Sci 2008;327:125–8.
[30] Lago M, Araujo M. Capillary rise in porous media. Physica A 2001;289:1–17.
[31] Masoodi R, Pillai KM, Varanasi PP. Darcy's law based models for liquid absorption in polymer wicks. AIChE J 2007;53(11):2769–82.
[32] Ramon G, Oron A. Capillary rise of a meniscus with phase change. J Colloid Interface Sci 2008;327:145–51.
[33] Polansky J, Kaya T. An experimental and numerical study of capillary rise with evaporation. Int J Therm Sci 2015;91:25–33.
[34] Lukas D, Soukupova V. Recent studies of fibrous materials wetting dynamics. In: INDEX 99 Congress, Geneva, Switzerland.
[35] Masoodi R, Pillai KM, Varanasi PP. Role of hydraulic and capillary radii in improving the effectiveness of capillary model in wicking. In: Proceedings of FEDSM2008 2008 ASME Fluids Engineering Conference, Jacksonville, Florida, USA.
[36] Quintard M, Whitaker S. Two-phase flow in heterogeneous porous media: the method of large-scale averaging. Transp Porous Media 1988;3:357–413.
[37] Lasseux D, Quintard M, Whitaker S. Determination of permeability tensors for two-phase flow in homogeneous porous media: theory. Transp Porous Media 1996;24:107–37.
[38] Al-Shareef A, Neogi P, Bai B. Force based dynamic contact angles and wetting kinetics on a Wilhelmy plate. Chem Eng Sci 2013;99:113–7.
[39] Rame E. The interpretation of dynamic contact angles measured by the Wilhelmy plate method. J Colloid Interface Sci 1997;185:245–51.
[40] Lemmon E, Huber M, McLinden M. REFPROP: Reference fluid thermodynamic and transport properties. In: NIST Standard reference database 23, Version 9.0.
[41] Eckels Engineering Inc. CryoComp, Version 5.1, 2010.
[42] Schnelle W, Engelhardt J, Gmelin E. Specific heat capacity of Apiezon N high vacuum grease and of Duran borosilicate glass. Cryogenics 1999;39(3):271–5.
[43] Hartwig JW. Screen channel liquid acquisition device bubble point test in liquid nitrogen. Cryogenics 2016;74:95–105.
[44] Hartwig J, McQuillen J. Analysis of screen channel LAD bubble point tests in liquid methane at elevated temperature. In: AIAA-2012-0759.